Electrochimica Acta 550 (2026) 148093

Contents lists available at ScienceDirect

Electrochimica Acta

journal homepage: www.journals.elsevier.com/electrochimica-acta

A semiempirical model for predicting magnesium alloy biodegradation in simulated body fluids: Influence of electrolyte composition and implant geometry

V. Verro [a], F. Di Franco [a,*], D. Pupillo [b], M. Santamaria [a]

[a] Dipartimento di Ingegneria, Università degli Studi di Palermo, 90128 Palermo, Italy
[b] Istituto di tecnologie avanzate per l'energia "Nicola Giordano", Consiglio Nazionale delle Ricerche (CNR-ITAE), 90126 Messina, Italy

A R T I C L E I N F O

Keywords:
Magnesium alloys
Biomedical
Simulated body fluids
Hydrogen evolution
Gas chromatograph
Predictive model
FEM

A B S T R A C T

A semiempirical model was developed to predict the biodegradation behavior of AZ31 magnesium alloy in simulated physiological environments. The corrosion performance of the alloy was evaluated in four solutions—Hank's Balanced Salt Solution (HBSS), Dulbecco's Modified Eagle Medium (DMEM), Kokubo solution, and 0.9 % NaCl—by combining electrochemical techniques, hydrogen evolution measurements via gas chromatography, and mass loss analysis. The results showed a strong dependence of corrosion kinetics and mechanisms on electrolyte composition. Generalized corrosion dominated in HBSS and DMEM due to phosphate layer formation, while localized attack was observed in Kokubo and saline media. Power-law degradation rates, derived from hydrogen evolution data, were incorporated into a finite element model of a fibula plate to predict mechanical property loss over time. The model was also applied to a stannate-based conversion coating (CC60), which delayed degradation and reduced early hydrogen release. This framework enables reliable prediction of in vitro implant performance based on corrosion environment and geometry, offering a practical tool for biodegradable implant design.

1. Introduction

Metallic biomaterials are extensively used as temporary or permanent implants in orthopaedic and cardiovascular applications, such as bone plates, screws, and vascular stents [1–5]. However, permanent metallic implants can lead to long-term complications, including chronic inflammation, thrombosis, restenosis, and the need for additional surgery to remove the implant once healing is complete [6–8]. In contrast, biodegradable metals, particularly magnesium and its alloys, have emerged as promising candidates for next-generation bioresorbable implants due to their favourable mechanical properties (e.g., low density, elastic modulus close to that of bone) and their ability to gradually corrode in the physiological environment, eliminating the need for implant removal [9–14].

Despite their potential, the clinical translation of magnesium-based implants remains limited, primarily due to their rapid and uncontrolled corrosion in chloride-rich environments like simulated body fluids (SBFs) [15–18]. The high degradation rate can compromise the mechanical integrity of the implant before tissue healing is completed. Moreover, the hydrogen gas evolution accompanying the corrosion process can result in gas pocket formation and localized alkalization, both of which may be detrimental to surrounding tissues [19–24].

Accurate estimation of the corrosion or dissolution rate of Mg alloys is therefore crucial for the design and safe application of biodegradable implants. Traditional electrochemical methods such as Tafel extrapolation are often used to evaluate corrosion kinetics. However, in the case of magnesium, these methods tend to underestimate the actual degradation rate due to the so-called negative difference effect (NDE), wherein the hydrogen evolution rate increases with anodic polarization—a behaviour not captured by Tafel analysis [25–30].

In addition, an often overlooked but critical factor is the composition of the electrolyte used to simulate the physiological environment. Various simulated body fluids (such as Dulbecco's Modified Eagle Medium [DMEM], Hank's Balanced Salt Solution [HBSS], saline solution or Kokubo solution) differ significantly in ion concentrations, buffering capacity, and organic content, all of which can strongly influence the degradation mechanisms and rates of Mg alloys [31,32]. Consequently, data obtained in one simulated fluid may not be directly transferrable to

---

* Corresponding author.
E-mail address: francesco.difranco@unipa.it (F. Di Franco).

https://doi.org/10.1016/j.electacta.2025.148093
Received 20 October 2025; Received in revised form 5 December 2025; Accepted 29 December 2025

another, emphasizing the necessity for experimental validation in multiple relevant media.

To address these challenges, gas collection methods, particularly hydrogen evolution rate measurements using gas chromatography (GC), provide a more direct and reliable estimate of the degradation behaviour of Mg alloys in vitro. By systematically quantifying the H_2 evolution in a range of physiologically relevant SBFs, it becomes possible to correlate the measured degradation rate with implant geometry and surface area, ultimately allowing for semiempirical modelling of implant lifetime as a function of shape, degradation environment, and physiological healing time.

The aim of this work is to develop a semiempirical calculation tool for estimating the dissolution rate of magnesium alloys used in biodegradable implants. To achieve this, we first perform a systematic experimental investigation of Mg alloy degradation in various simulated body fluids, including commonly used solutions such as Saline solution, Dulbecco’s Modified Eagle Medium, Hank’s Balanced Salt Solution, and Kokubo solution. Hydrogen evolution rates are measured using gas chromatography, providing accurate, quantitative data on the dissolution kinetics of Mg in each medium. The results are then used to construct a semiempirical model that relates the implant geometry, surface area, degradation environment, and healing time to the expected corrosion rate. This approach aims to overcome the limitations of electrochemical methods such as Tafel extrapolation, while providing a practical predictive tool for the design and optimization of magnesium-based biodegradable implants.

2. Materials and methods

2.1. Preparation of samples

Squared samples of AZ31 Mg alloy (Mg 96 %, Al 3 %, Zn 1 %, Goodfellow) were obtained from a 1 mm thick sheet. The surface of the samples was prepared with a mechanical grinding, using silicon carbide paper (Buehler) with progressively higher grit number, up to P2500. During this process, samples were quenched in ethanol ($C_2H_6O \geq 99.5$ % - Emplura). Afterwards, AZ31 coupons were cleaned in an ultrasonic bath with ethanol for 10 min, and finally dried in air.

2.2. Testing solutions

Testing solutions used for both immersion and electrochemical tests are reported in Table 1. The solutions were prepared in our laboratory except for the Dulbecco's Modified Eagle Medium (DMEM with stable Glutamine, with 1.0 g L^{-1} Glucose – Genaxxon bioscience). All solutions were maintained at 37 °C for the whole duration of the tests in order to mimic physiological environment.

Such solutions were used as testing electrolyte for both electrochemical characterization and H_2 evolution measurements (see below).

2.3. Electrochemical measurements

In order to assess the Mg alloy behaviour in the different testing solutions, electrochemical measurements have been carried out on at least 3 identical samples, maintaining the physiological temperature of 37 °C. The adopted setup included a Parstat 2273 potentiostat and an electrochemical cell with a three-electrode configuration, with an Ag/AgCl/sat. KCl reference electrode and a platinum mesh as the counter.

Table 1
Testing solutions Compositions. (*) Participating in the pH Buffer Mechanism.

Saline solution		HBSS		Kokubo		DMEM	
substance	*conc. (mg L^{-1})*	*substance*	*conc. (mg L^{-1})*	*substance*	*conc. (mg L^{-1})*	*substance*	*conc. (mg L^{-1})*
NaCl	9000	NaCl	8000	NaCl	7990	NaCl	6400
		KCl	400	KCl	230	KCl	400
		(*) $NaHCO_3$	300	(*) $NaHCO_3$	350	$CaCl_2$	200
		(*) Na_2HPO_4	60	(*) K_2HPO_4 $3H_2O$	230	$MgSO_4$ $7H_2O$	200
		(*) NaH_2PO_4 H_2O	250	$MgCl_2$ $6H_2O$	300	(*) Na_2HPO_4	124
		$MgCl_2$	190	$CaCl_2$ $2H_2O$	360	D-Glucose	1000
		$CaCl_2$ $2H_2O$	190	Na_2SO_4	70	$Fe(NO_3)_3$ H_2O	0.1
		$MgSO_4$ $7H_2O$	60	HCl (1 M)	≈40 mL	Na-Pyruvate	110
		Glucose	1000	(*) Tris	6044.7	Phenol red	15
						(*) $NaHCO_3$	3700
						L-Arginine HCl	84
						L-Cysteine	48
						L-Glutamine	580
						L-Histidine HCl	42
						L-Isoleucine	106
						L-Leucine	106
						L-Lysine HCl	146
						L-Methionine	30
						L-Phenylanine	66
						L-Threonine	95
						L-Tryptophan	16
						L-Tyrosine	72
						L-Valine	94
						Glycine	30
						L-Serine	42
						Cholinchloride	4
						Folic acid	4
						Myo-Inositol	7.2
						Nicotinamide	4
						Da-Ca-Pantothenate	4
						Pyridoxal HCl	4
						Riboflavin	0.4
						Thiamine-HCl	4

Open circuit potential (OCP) was measured over time, electrochemical impedance spectroscopy (EIS) was adopted, EIS was measured at the OCP, varying the potential in the range ± 10 mV; and investigating frequencies between 10 mHz and 100 kHz (5 points per decade). For each sample, polarization curves were obtained with a 5 mV/s scan rate and a potential sweep between −0.15 V vs OCP and −0.50 V vs SSC.

2.4. H_2 evolution measurements

Hydrogen evolution rate evaluation was carried out by immersing samples individually in closed bottles, with a stopper in bromobutyl rubber. Gas samples were collected with a 500 µL Hamilton gastight syringe. The bottles were kept in an incubator, maintaining the physiological temperature of 37 °C. For each experiment, the ratio between solution volume and immersed area was 25 ml/cm^2, the solutions were changed after 3.5 days from the beginning of each test and gas samples were collected periodically during a 7-day period. The collected samples were analysed with a HP 6890 Series gas chromatograph.

A gravimetric analysis was also conducted. The mass of the samples was measured with a (Kern analytical balance ACS 120–4) scale before the 7-days immersion and after the removal of corrosion product (see below).

2.5. Surface analysis

FT-IR analysis was also carried out, using a FT-IR/NI Spectrum 400 spectrophotometer (Perkin Elmer, Waltham, MA, U.S.A.), in the range 4000–500 cm^{-1}.

Corrosion products were removed from the surface of the samples after the H_2 evolution test, in accordance with ASTM G1–03 [33]. Samples first rinsed in DI water, then they were immersed in an aqueous solution of 200 g L^{-1} chromium (VI) oxide (Sigma Aldrich, ≥98.0 %) and 2 g L^{-1} silver nitrate (VWR Chemicals, ACS analytical reagent) for 5 min, then cleaned in an ultrasonic bath for 5 min in DI water and finally rinsed in ethanol and left to dry at room temperature.

Each sample was analysed by means of scanning electron microscopy, using a FEI Quanta 200 FEG SEM instrument, with an EDX probe. SEM micrographs were acquired before and after the removal of corrosion products from the surface of the samples.

2.6. FEM analysis

A model of an orthopedic fibula plate was created and subjected to a simulated four-point bending test, in accordance with ASTM F382 [34]. The test was performed using finite element analysis (FEA) software to simulate static structural conditions. Multiple geometric variations of the 3D model were tested to assess the plate's mechanical properties over its expected service life. The design of the fibula plate was based on a simplified version of commercially available plates [35–37], with the dimensions and bending test parameters detailed in Fig. 1.

Material properties adopted in the model to simulate AZ31 alloy were selected from the native database in the FEM software and are reported in Table 2.

The initial geometry was discretized with 0.2 mm tetrahedrons, obtaining $N = 135{,}479$ elements, with an average skewness of $S_{avg} = 0.43$.

3. Results and discussion

3.1. Testing solutions composition

The corrosion rate of AZ31 samples was estimated using various physiological solutions, since the solution selection significantly affects corrosion experiment results [38]. Saline solution, Kokubo solution, Hank's Balanced Salt Solution (HBSS), and Dulbecco's Modified Eagle Medium (DMEM) were employed. Saline solution (the simplest physiological medium) contains only 9 g L^{-1} of NaCl and lacks buffering agents to stabilize local pH. Both Kokubo solution and HBSS contain calcium ions, carbonates, phosphates, and sulphates. Kokubo solution utilizes Tris/HCl as a buffering agent, though it has been shown to be ineffective at stabilizing local pH [39]. In contrast, HBSS contains a high amount of phosphate ions, which are capable of stabilizing local pH. Finally, DMEM is a highly complex cell culture medium, which, in addition to inorganic ions, also contains amino acids, vitamins, glucose, and other essential nutrients for cell growth.

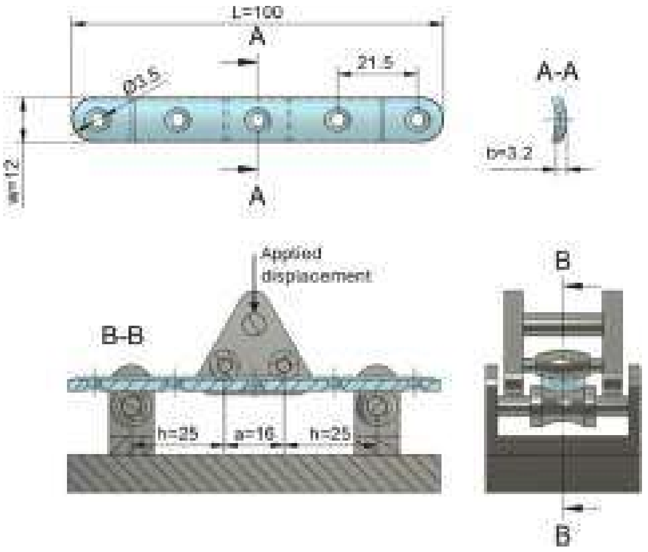

Fig. 1. Fibula plate dimensions and four-point bending test setup as described in ASTM F382 (length are expressed in *mm*).

Table 2
AZ31 mechanical properties in the FEM model.

Material properties		
Density	1770	kg m^{-3}
Young's Modulus	45	GPa
Poisson's Ratio	0.35	
Bulk Modulus	50	GPa
Shear Modulus	17	GPa
Yeald Strength	193	MPa
Tangent Modulus	920	MPa

3.2. Morphology

The morphology of samples surface after 7 days immersion in the different testing solutions has been analysed by SEM. Fig. 2 shows the micrographs of AZ31 samples immersed for 168 h in the four testing solutions. For samples immersed in HBSS a characteristic "mud" structure is visible, consisting of a cracked layer of corrosion products [31, 40]. Also, it can be seen that the degradation of the surface was mainly due to a general form of corrosion, and its products covered the sample with particles agglomerate uniformly distributed. EDX analysis (Table 3) shows that the corrosion product layer is mainly constituted by Ca, P and C.

SEM micrograph of sample immersed in DMEM also shows mud structure, with uniform degradation and corrosion product distribution. Notably, particle agglomeration was almost absent on these samples. SEM micrographs of a sample immersed in Kokubo solution for 7 days show that both the mud structure and few particle agglomerates are present. Moreover, much more degradation occurred. For samples immersed in NaCl 0.9 % solution, it is shown vast presence of corrosion products, without any visible mud structure.

FT-IR spectra for samples after 7-days immersion at 37 °C in

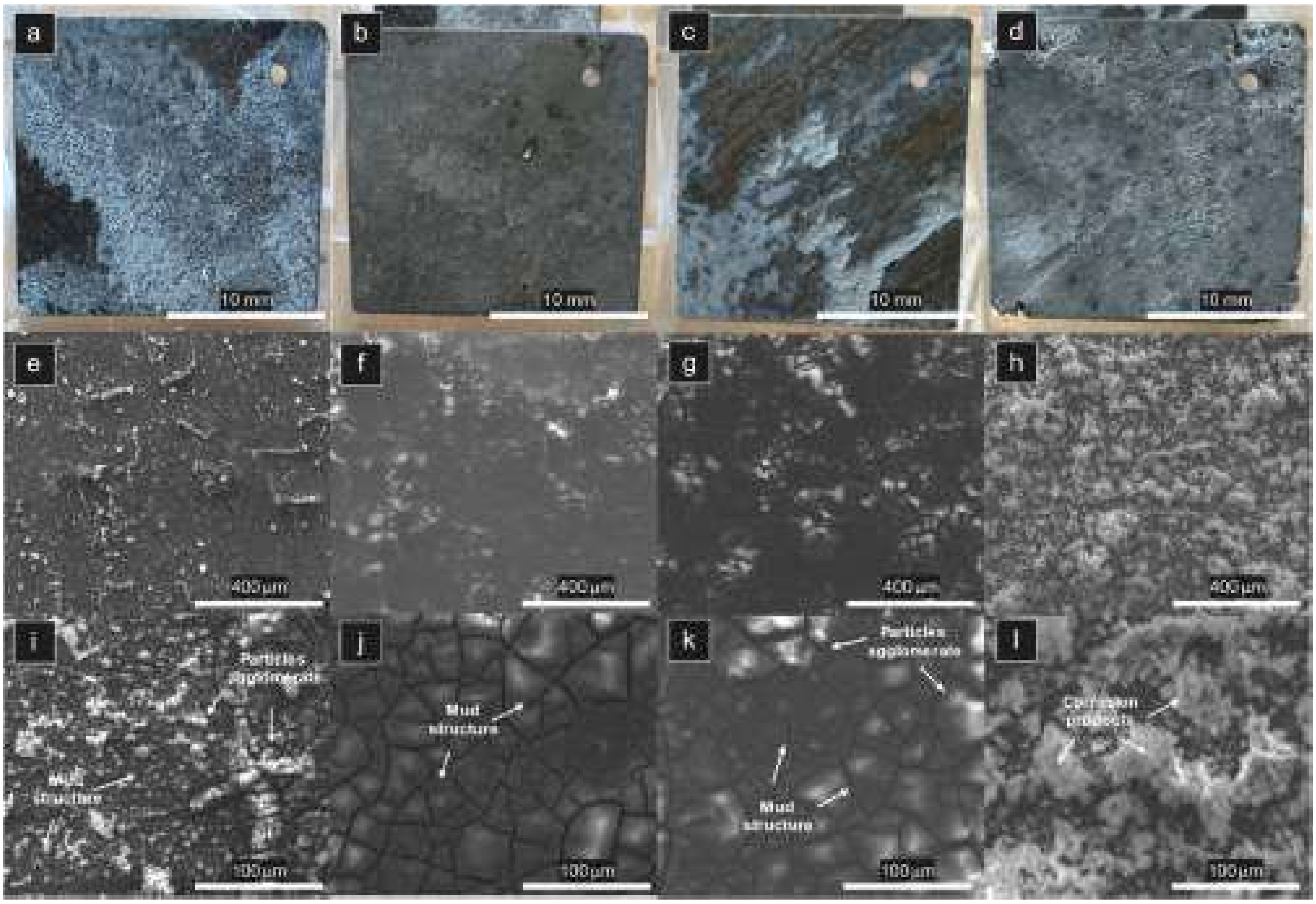

Fig. 2. Pictures SEM micrographs of AZ31 samples after 7-days immersion: a-e-i) HBSS, b-f-j) DMEM, c-g-k) Kokubo, D-h-l) NaCl 0.9 %.

Table 3
EDX analysis of AZ31 samples after 168 h of immersion in the four testing solutions.

At.%	HBSS *t* = *168* h	DMEM	Kokubo	NaCl 0.9 %
C	16.9	18.34	17.01	-
O	37.68	35.29	50.47	63.08
Zn	0.29	0.4	0.51	0.17
Mg	28.17	36.87	10.8	35.87
Al	0.62	3.23	3.17	0.15
Na	0.64	0.49	1.31	0.36
Cl	-	-	-	0.38
P	9.02	3.99	10.22	-
Ca	6.67	1.40	6.51	-

physiological solutions are shown in Fig. 3. The spectra reveal strong bands at 1020 cm^{-1} and at 570 cm^{-1} corresponding to PO_4^{3-} stretching and bending modes, respectively, indicating the precipitations of phosphate layers. The latter is further confirmed by the presence of a band at 3000–3600 and 1630 cm^{-1} that according to the literature can be associated to the presence of water in phosphates [41]. For AZ31 immersed in DMEM the asymmetric stretching vibrations of CO_3^{2-} at 1485 cm^{-1} and 1426 cm^{-1} are evident [42], suggesting the precipitation of carbonate in agreement with the high concentration of $NaHCO_3$ in this solution (see Table 3). Smaller bands at the same wavelengths are also present for HBSS and Kokubo, i.e. in the physiological media containing a lower concentration $NaHCO_3$.

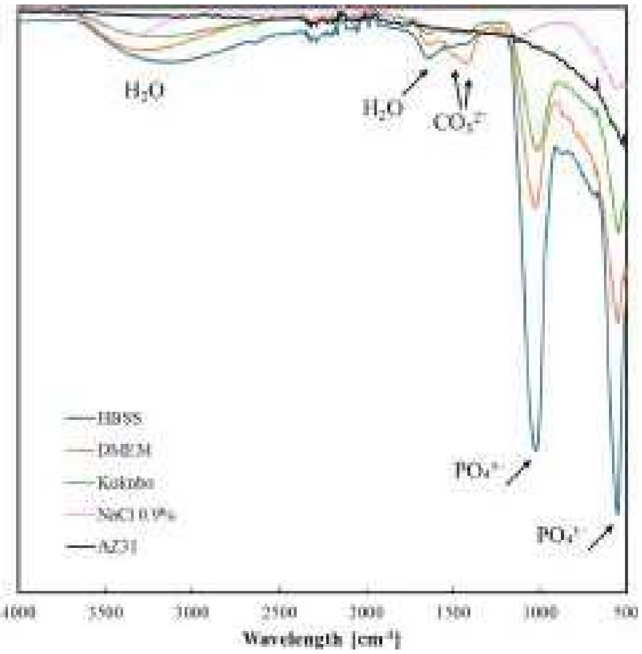

Fig. 3. FT-IR analysis on AZ31 samples, before and after 168 h of immersion.

3.3. *Electrochemical characterization*

In order to assess corrosion behaviour of tested samples in the different simulating solutions, electrochemical testing techniques were adopted. The electrochemical measurements for samples that had been immersed for 7 days were conducted immediately after removing the samples and placing them in a new solution with the same composition as the immersion test solution. Open circuit potential was recorded over time for AZ31 samples in the respective solution, the values reported in Table 4 were reached after a 1 h stabilization time.

Samples immersed in HBSS showed the highest OCP, with no changes after the immersion period.

Impedance spectra, reported in Nyquist representation in Fig. 4 and in Bode representation in Figure S1, were collected after 1 h and after 168 h of immersion in the different media. The impedance spectra displayed in Fig. 4a, presented in the Nyquist format, exhibit at least two distinct time constants along with an inductive loop.

The presence of phosphates led to the formation of a conversion coating that protect the surface, as it can be seen with the increasing overall impedance after 7 days immersion (~ 6 to ~20 kΩ cm^2). OCPs in DMEM were the lowest, with no significant changes over the 7 days. Nyquist plots for samples immersed in DMEM are reported in Fig. 4b Here it can be seen that no substantial variation occurred after 7 days, being the overall impedance around 2 kΩ cm^2, with a non-entirely formed inductive loop at low frequencies. Samples immersed in Kokubo solution showed the highest variation in recorded OCPs (+120 mV) and the lowest corrosion resistance (i.e. overall impedance) among the different solutions (Fig. 4c). A second time constant appeared in the Nyquist representation of the EIS spectra, both before and after the 7-days immersion, with an increase of one order of magnitude of the overall impedance (120 to 1000 Ω cm^2), and with the clear presence of the inductive loop at the low frequencies in these plots. Sample tested at $t = 1$ h in NaCl 0.9 % solution showed the clearest inductive loop at low frequencies as well as a capacitive loop, with an overall impedance of <350 Ω cm^2 (Fig. 4d) and an OCP of −1.54 V. After 7 days of immersion, the loop nearly disappeared, accompanied by an increase in overall impedance to approximately 2500 Ω cm^2 and a recorded OCP of −1.50 V.

Fitting such complex spectra requires kinetic models that describe reactions involving the formation of adsorbed intermediates followed by its subsequent oxidation, as extensively detailed in reference [43]. However, a survey of already published literature allows to find an equivalent circuit that has been used to fit the EIS spectra in HBSS, DMEM and Kokubo solutions (see Fig. 5a) [44,45]. A parallel between a constant phase element, Q_1, and the series between a resistance, R_1, and an inductance, L_1, were introduced to account for the corrosion of Mg alloys with simultaneous hydrogen evolution. Notably, Q_1 accounts for the non-ideal capacitance of alloy/electrolyte interface. However, during immersion at the open circuit potential in physiological solutions a phosphate and/or carbonate layer precipitates on the alloy surfaces inducing the formation of a not compact passive film, whose presence is modelled by the series between Q_3 and R_3 parallel accounting for its capacitance and resistance. Finally, R_2 accounting for the electrolyte resistance in this porous layer [46]. In the case of 0.9 % NaCl solution, there is no evidence of conversion layer contribution to the measured impedance (in agreement with SEM images of Fig. 4d, h, l), thus the simpler equivalent circuit of Fig. 5b where the R_3Q_3 parallel was removed. This circuit is coincident with that reported in ref [30]., that has been derived from a kinetic model accounting for the formation of adsorbed intermediates for both the anodic half-cell reaction (magnesium oxidation) and the cathodic half-cell reaction (hydrogen evolution).

Table 4
Recorded open circuit potential of AZ31 samples.

OCP [V vs SSC]	HBSS	DMEM	Kokubo	NaCl 0.9 %
$t = 1$h	−1.52	−1.69	−1.63	−1.54
$t = 168$h	−1.52	−1.62	−1.51	−1.50

The fitting parameters are reported in Table 5. It is noteworthy that the contribution of the conversion layer to the overall impedance is significant for the spectra recorded in HBSS and DMEM, and this behaviour is observed consistently at both short (1 h) and long (168 h) immersion times. In contrast, for Kokubo solution, R_3remains very low and Q_3very high at both exposure durations. Regarding the $L_1 - -R_1$branch associated with the corrosion reaction, the values obtained for HBSS, DMEM, and Kokubo are comparable to those reported in the literature (e.g., ref [30]), while a very low inductance L_1 is consistently estimated in 0.9 % NaCl solution. Because the magnitude of L_1 depends on the kinetics of both hydrogen evolution and magnesium oxidation, explaining this behavior is not straightforward. Nevertheless, it may be suggested that passivation in 0.9 % NaCl solution is more complex, resulting in a more continuously renewing passive surface throughout the experiments, regardless of immersion time.

Polarization curves recorded in HBSS (Fig. 6a) after 7 days of immersion indicate a reduction in current density in the anodic branches, which can be attributed to the formation of a thick phosphate conversion coating. This is accompanied by a shift in corrosion potential by almost 100 mV, along with an increase in pitting potential. In contrast, curves recorded in DMEM solution (Fig. 6b) show minimal changes in current densities across both the anodic and cathodic branches after 168 h. However, there is an increase of approximately 100 mV in both corrosion and pitting potentials following the 7-day immersion. Polarization curves obtained in Kokubo solution (Fig. 6c) reveal the most significant variation, with the current density in the anodic branch changing by more than an order of magnitude. This is coupled with an almost 100 mV increase in both corrosion and pitting potentials. Lastly, polarization curves for samples immersed in 0.9 % NaCl solution (Fig. 6d) show a decrease in corrosion potential of approximately 100 mV, along with an increase in pitting potential in the anodic region. Notably, the shift in the corrosion potential according to polarization curves for the samples after 168 h immersion in all the electrolytes, can be explained by the presence of the conversion layer or of the corrosion products, even if we cannot exclude that the cathodic polarization (and the consequent slightly alkalinization) played a role.

3.4. *Corrosion products removal*

After the removal of corrosion products from the surface of samples immersed in the different solutions, EDX analysis was carried out in order to verify the effectiveness of the procedure. EDX results are reported in Table 6, where no other elements were present other than oxygen and the alloy constituents. These results can also be confirmed by SEM micrographs of the samples (Fig. 7). A comparison with Table 3 and Fig. 2 shows that corrosion product (mainly phosphate and carbonate), were effectively removed from the surfaces.

SEM micrographs of samples in HBSS solution after corrosion products removal (Fig. 7a-b) confirmed the effects of a mostly generalized corrosion attack on the surface, along with the presence of a few pits. Such behaviour is probably due to the formation of a protective layer (the thick mud structure seen in Fig. 2i), that prevents a more aggressive form of corrosion. Immersion in DMEM led to a more pronounced degradation of the samples with respect to HBSS's, as it can be seen in Fig. 7b-f, with the formation of a rough but still homogeneous surface. Micrographs in Fig. 7c-g show the widely degraded surface of a sample immersed in Kokubo solution for 7 days after corrosion product removal. On the surface it can be seen a large number of pits, which grew larger and merged together forming deep cavities. This phenomenon was significantly more pronounced compared to what was observed in the other testing solutions. In Fig. 7d-h is shown the surface of a sample immersed in NaCl 0.9 % after corrosion product removal. It can be seen that also here many pits are present, but they appear smaller than what observed in the Kokubo solution. Such pits formation and distribution led to a slightly more regular surface than with Kokubo's, even with the presence of numerous deep cavities. The removal of corrosion products

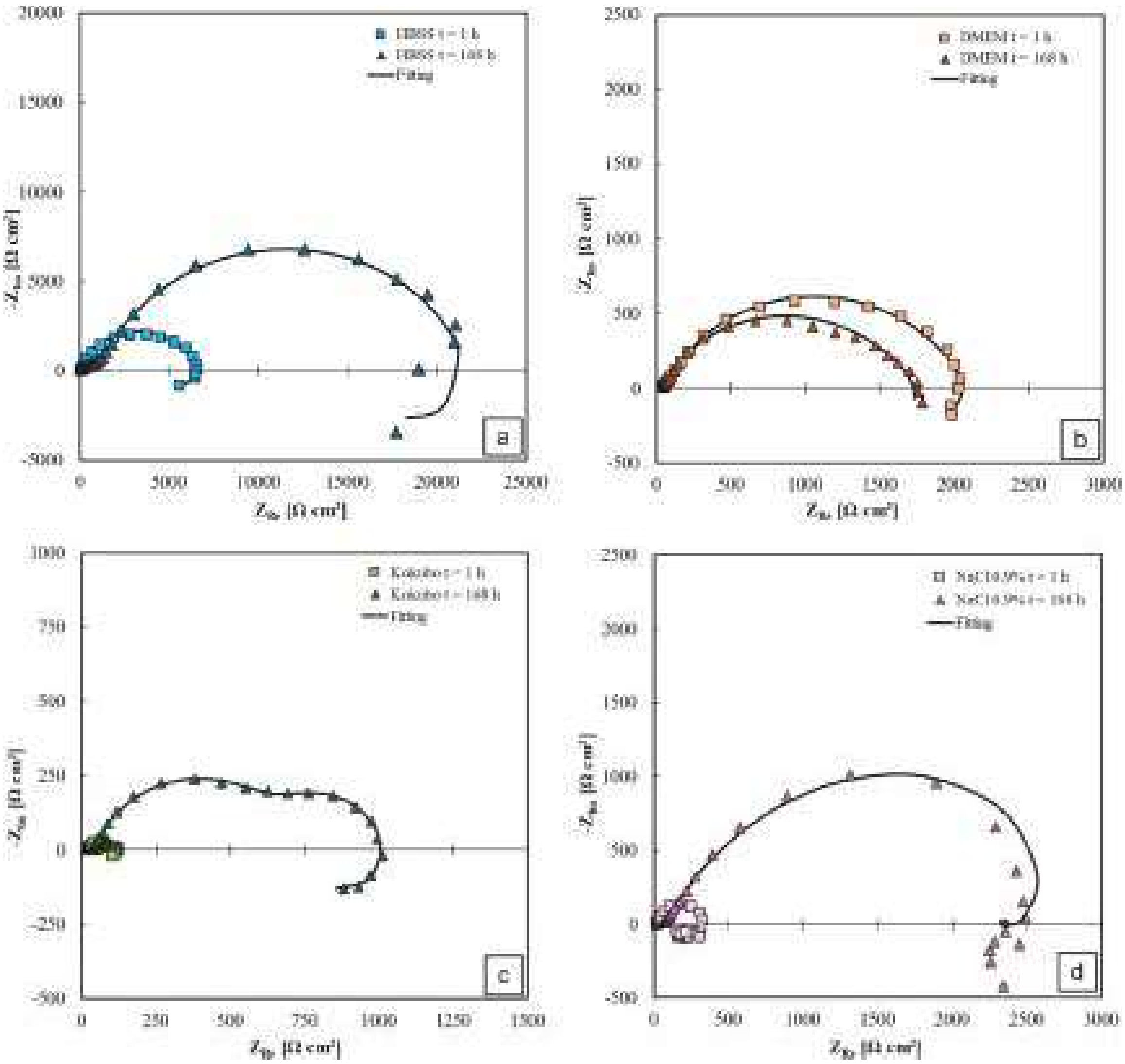

Fig. 4. Nyquist representation of EIS of AZ31 samples in testing solutions after 1 and 168 h of immersion in: a) HBSS, b) DMEM, c) Kokubo, d) NaCl 0.9 %.

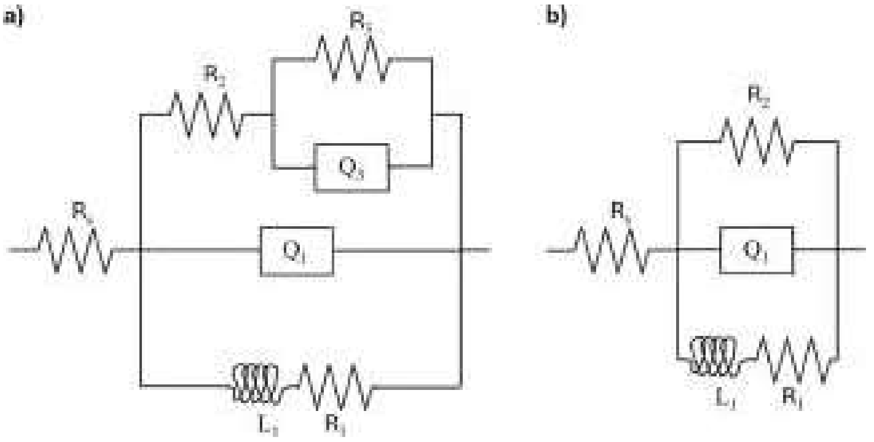

Fig. 5. Equivalent electric circuits used for the fitting of EIS spectra recorded in a) HBSS, DMEM, Kokubo and b) NaCl 0.9 % solutions.

allowed to identify a localized form of corrosion in Kokubo and NaCl solutions.

3.5. *Hydrogen evolution estimation*

Hydrogen evolution is the primary cathodic reaction occurring during Mg alloys corrosion, thus obtaining a precise evaluation of its entity is of great importance in assessing corrosion behaviour. In Fig. 8

Table 5
Fitting parameters related to EIS of AZ31 samples in testing solutions after 1 and 168 h of immersion.

		HBSS *t = 1h*	*DMEM* *t = 1h*	*Kokubo* *t = 1h*	*NaCl 0.9 %* *t = 1h*
R_s	(Ω cm^2)	17	26	18	22
Q_1, n	(μS s^n cm^{-2})	20, 0.71	25, 0.62	36, 0.82	14, 0.93
R_1	(Ω cm^2)	1.9×10^4	8.3×10^3	1.8×10^2	4.3×10^2
L_1	(Ω s cm^2)	5.0×10^5	1.0×10^5	4.4×10^3	80
R_2	(Ω cm^2)	2.6×10^2	6.6×10^1	7.5×10^1	3.2×10^2
R_3	(Ω cm^2)	6.3×10^3	2.0×10^3	2.4×10^1	-
Q_3, n	(μS s^n cm^{-2})	2, 0.98	15, 0.77	2760, 0.98	- -
		HBSS t = 168h	***DMEM t = 168h***	***Kokubo t = 168h***	***NaCl 0.9 % t = 168h***
R_s	(Ω cm^2)	10	38	41	73
Q_1, n	(μS s^n cm^{-2})	3, 0.60	66, 0.60	40, 0.77	28, 0.67
R_1	(Ω cm^2)	5.5×10^4	1.0×10^3	2.5×10^3	6.2×10^3
L_1	(Ω s cm^2)	9.1×10^5	2.0×10^5	4.3×10^5	8.0×10^2
R_2	(Ω cm^2)	1.1×10^3	1.0×10^2	6.8×10^2	3.7×10^3
R_3	(Ω cm^2)	2.1×10^3	1.6×10^3	3.0×10^2	-
Q_3, n	(μS s^n cm^{-2})	8, 0.74	3, 0.99	880, 0.91	- -

are reported the H_2 evolution rates. These corrosion rates were calculated as the slope of the interpolating straight line obtained plotting the hydrogen evolution (ml cm^{-2}) measured in the gas samples collected at different times (expressed in days) (see figure S2).

It can be seen that in HBSS almost no H_2 evolution is recorded in the first 6 h, while the corrosion rate has a maximum during the first day and then starts to decrease. The hydrogen evolution data for samples in DMEM show that the highest rate is recorded in the first 6 h then it rapidly reduces until after 7 days when it's less than half the initial value. This trend is not observed in the measured overall impedance, since it is related to the formation of a thin conversion coating layer, thus confirming that estimating corrosion rates by electrochemical measurements only could be misleading.

Electrochemical measurements showed the highest corrosion rate in Kokubo solution, which is attributed to its lower concentration of phosphate ions and reduced buffering capacity compared to DMEM and HBSS media. Such behaviour is reflected also in the hydrogen rates. After an initial burst in the first six hours, where the measured HER was nearly 6 ml cm^{-2} days^{-1}, the evolution rate decreases with a halving time of ~7 days.

In NaCl solution, the rate of H_2 evolution is higher than that observed in HBSS and DMEM due to the complete absence of phosphates and other species capable of forming a protective layer. However, this rate is lower compared to that measured in Kokubo solution, due to the lack of buffering agents to mitigate pH increase. Consequently, the pH in NaCl solution rises rapidly, resulting in partial passivation of the sample surface (see Figure S3).

3.6. *Mass loss evaluation*

The hydrogen evolution rates obtained for samples in the different testing solutions were used to evaluate the corresponding expected mass loss due to Mg oxidation during the 7-day immersion period, with the hypothesis of no other concurring reactions. This is calculated by assuming that all the hydrogen detected with the gas chromatograph origins from Mg dissolution, according to the following reactions:

$$Mg \rightarrow Mg^{2+} + 2e^- \tag{5}$$

$$2H^+ + 2e^- \rightarrow H_2 \tag{6}$$

Magnesium mass loss is calculated by multiplying $\boldsymbol{n_{Mg}}$ (= $\mathbf{n}_{H2}$, the number of H_2 moles detected) and $\boldsymbol{MW_{Mg}}$ (24.305 g/mol the molecular weight of Mg), then dividing by the surface area of the immersed sample $\boldsymbol{A}$.

In addition, the gravimetric analysis of the samples allowed us to compare the mass loss (and thus the thinning rate knowing the alloy density) estimates with the actual mass variation after corrosion product removal. These results are reported in Fig. 9, where *indirect* Δm are obtained with GC and *direct* Δm are the mass losses measured with the scale. It can be seen that mass losses estimated by GC measurements were in good agreement with those measured after corrosion products removal. Moreover, Fig. 9 further confirms that the estimated corrosion rate is strongly affected by the physiological media used, since the different compositions can affect the corrosion mechanisms.

3.7. *FEM analysis*

The evaluation of the degradation rate of AZ31 alloy in different solutions allowed to try and predict its effectiveness as biomaterial for orthopaedic plates. The corrosion rates obtained were adapted to a realistic geometry of a fibula plate: such plates are not usually subjected to heavy loads, and the use of Mg alloys for such application appears feasible. The geometric modelling of the fibula plate was inspired by actual plates currently manufactured with stainless steel or Ti alloys [35–37].

In agreement with FDA regulations, the mechanical testing standard for metallic bone plates must follow ASTM F382 specification [34,47], consisting in a four-point bending test that was implemented in the structural simulation carried out with the finite element method. The minimum requirements described by FDA for fibula metallic plates are 2.3 N m Minimum Bending Strength and 0.17 N m^2 Minimum Bending Structural Stiffness.

The four-point bending test support was modelled in the FEM software by using suitable boundary conditions (BCs), in order to mimic the real test conditions (see Fig. 10).

A displacement of 2.5 mm was imposed along the Z direction on the segments named LP1 and LP2, while measuring the reaction forces in SC1 and SC2 in order to obtain a Force-Displacements diagram. Bending Strength and Bending Structural Stiffness of the modelled plate were calculated in accordance with ASTM F382, and results are reported in Table 7.

After this first test, the geometry of the plate was altered reducing its volume by imposing a negative offset, in the normal direction with respect to all the faces of the model. Such geometry modification was adopted in order to mimic a generalized form of corrosion, under the hypothesis of uniform material loss along all the plate. In Table 7 are reported a few of the investigated offset, along with the corresponding resisting volume and mechanical properties. It is important to notice that both bending strength and bending stiffness have to be over the minimum acceptable values, while the former appears to be the limiting constrain in this configuration.

The evaluation of hydrogen evolution rates in the four tested physiological media allowed to estimate the corrosion behaviour of the fibula plate in such solutions. The experimental recorded mass variation of the alloy as a function of the immersion time was fitted with a power law function ($y = ax^b$) and used to predict the corrosion behaviour for up to 180 days of immersion (see figure S4). The power laws were used to model fibula plate volume variation with time, and the corresponding mechanical properties were obtained as explained above, assuming uniform corrosion (see Fig. 11). The simulations show that an implant corroding in Kokubo medium would last only 7 days maintaining acceptable bending strength. Such duration is doubled in NaCl solution, while it would extend to over 60 days with the DMEM corrosion rate.

The previously described approach was also applied to model the effect of a protective coating on the AZ31 alloy substrate. In this case, a stannate-based conversion coating (referred to as CC60) was selected,

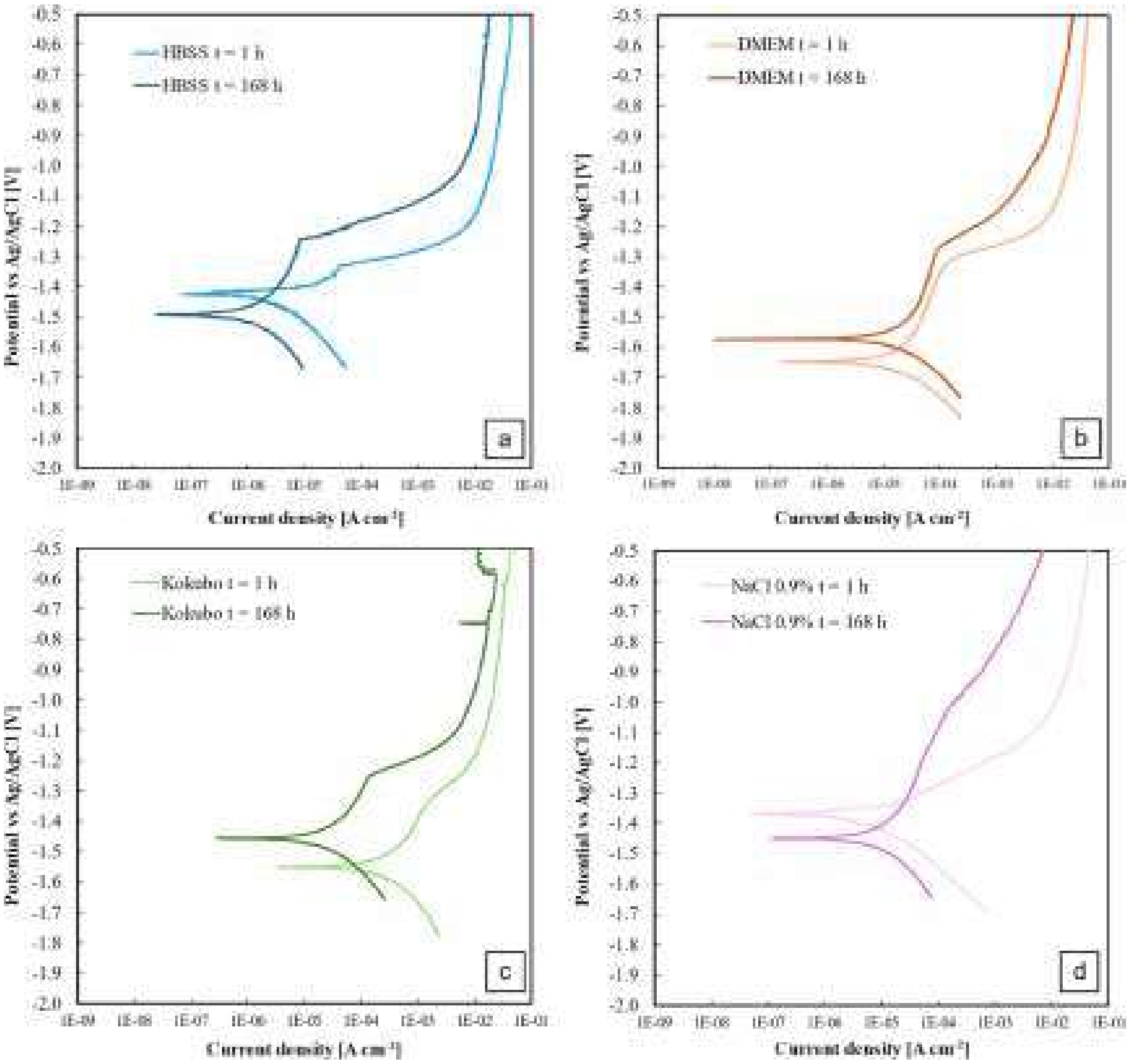

Fig. 6. Polarization curves of AZ31 samples in testing solutions before and after 168 h of immersion: a) HBSS, b) DMEM, c) Kokubo, d) NaCl 0.9 %.

Table 6
EDX analysis of AZ31 samples after the removal of corrosion products.

At. %	HBSS	DMEM	Kokubo	NaCl 0.9 %
O	2.93	3.57	2.83	3.91
Mg	94.77	94.45	94.63	93.21
Al	1.90	1.63	2.27	2.46
Zn	0.39	0.36	0.27	0.42

which was formed by treating the AZ31 alloy for 60 min in $(SnO_3)^{2-}$ containing bath. The biodegradation behaviour of this coating in DMEM was characterized in earlier research [48]. Based on hydrogen evolution measurements obtained via gas chromatography in DMEM, the corrosion rate of the coated alloy follows a power-law relationship, reported in figure S4.

This expression is valid until the coating is completely degraded. Once the underlying magnesium alloy is exposed to the environment, the corrosion rate is assumed to follow the same power law previously established for bare AZ31 in DMEM. The evolution of mechanical properties for the coated plate is illustrated in Fig. 12, which also provides a direct comparison with the uncoated alloy under the same conditions. The results suggest that the coating can extend the implant’s functional lifespan by approximately two weeks. Additionally, it offers the advantage of reduced hydrogen release during the initial post-implantation period—a critical phase often associated with inflammation risks.

The results show that modelling the time-dependent degradation of an implant in various simulated body fluids under a known load can be a robust methodology for predicting the evolution of mechanical integrity as a function of immersion time. This case study exemplifies how experimentally derived corrosion rates, when coupled with load-bearing requirements, can inform critical design choices such as implant geometry, size, and the necessity of surface coatings. The proposed approach enables a rational, data-driven pathway for the selection and optimization of biodegradable Mg alloy implants, offering a valuable tool for early-stage development and the design of patient-specific orthopaedic solutions.

4. Conclusions

The corrosion behaviour of AZ31 alloy was investigated in four different simulated body fluids by combining electrochemical testing with direct hydrogen evolution measurements (via gas chromatography) and mass loss analysis after removal of corrosion products. The findings highlight the significant impact of the physiological medium's composition on both the corrosion rate and the underlying corrosion mechanisms. In particular, the high phosphate concentration in HBSS promotes the formation of a protective conversion layer, which slows

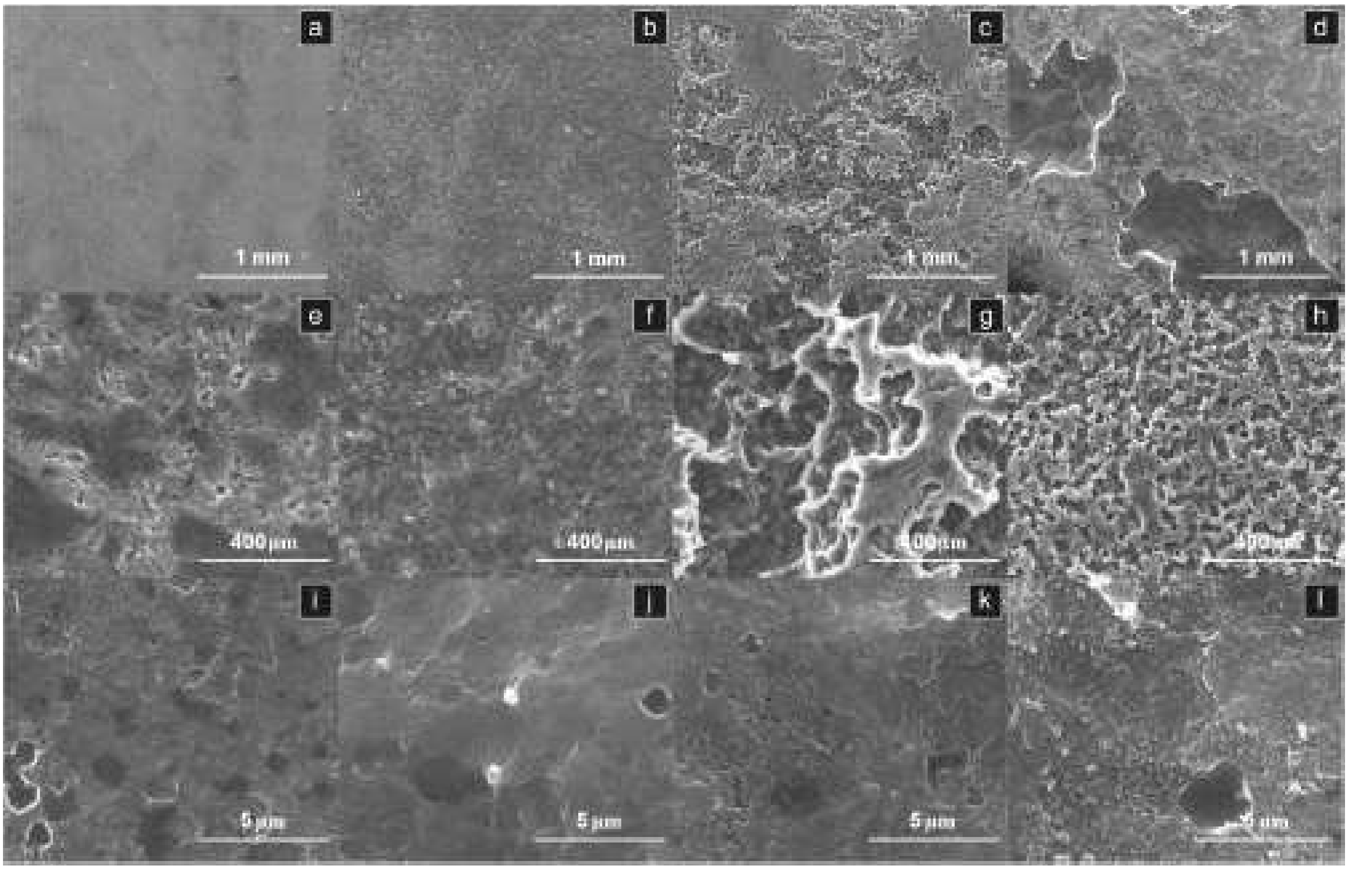

Fig. 7. SEM micrograph of AZ31 after immersion in the four test solutions and removal of corrosion products: a-e-i) HBSS, b-f-j) DMEM, c-g-k) Kokubo, D-h-l) NaCl 0.9 %.

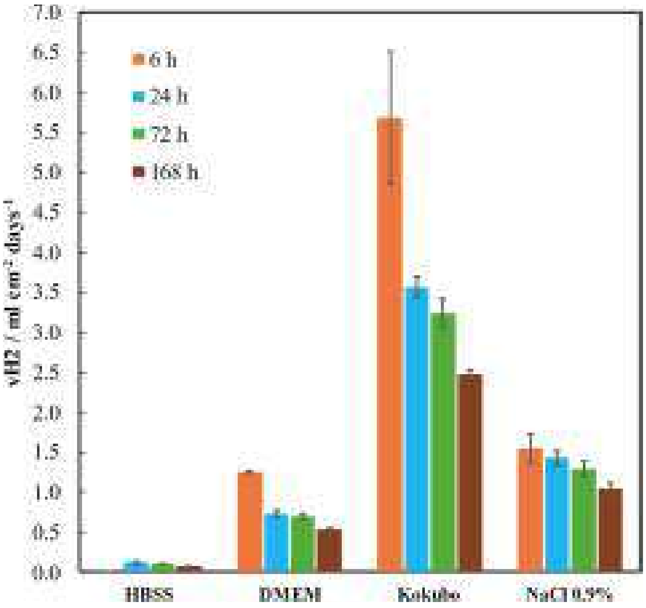

Fig. 8. Hydrogen evolution rate evaluated with GC measurements.

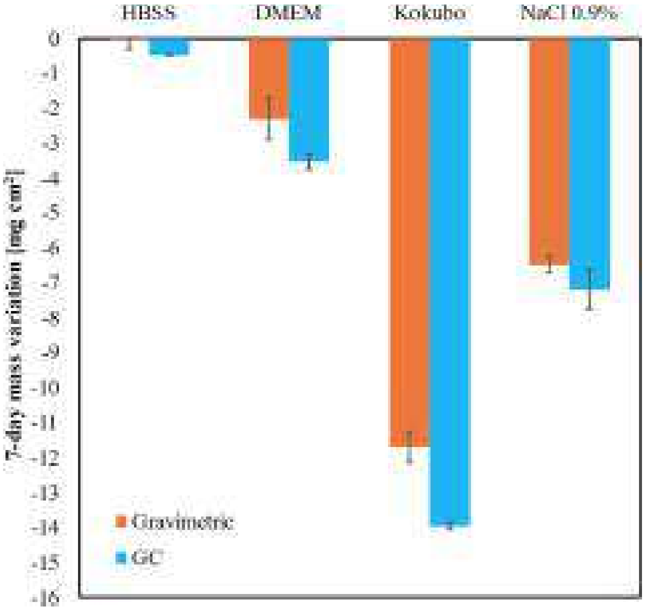

Fig. 9. Mass variation of AZ31 samples after 7 days of immersion as evaluated with gravimetric analysis and with gas chromatograph measurements.

down corrosion. SEM imaging after corrosion product removal revealed generalized corrosion in HBSS and DMEM, while localized corrosion was observed in Kokubo and saline solutions. An empirical biodegradation rate was experimentally derived as a function of immersion time, enabling prediction based on FEM analysis of the mechanical property evolution of AZ31 fibula plate during immersion in various physiological environments. This method was applied to both uncoated and coated samples. The results provide a useful framework for optimizing implant design—specifically, selecting component dimensions to ensure adequate mechanical support throughout the healing period, up to full tissue recovery.

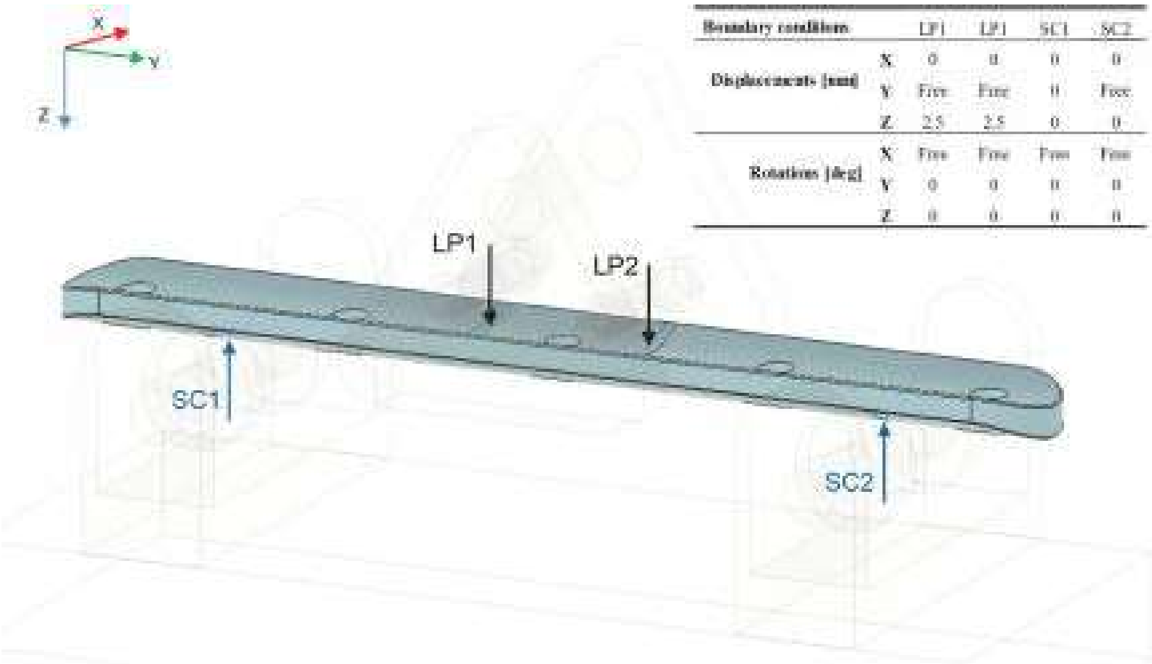

Boundary conditions		LP1	LP1	SC1	SC2
Displacements [mm]	X	0	0	0	0
	Y	Free	Free	0	Free
	Z	2.5	2.5	0	0
Rotations [deg]	X	Free	Free	Free	Free
	Y	0	0	0	0
	Z	0	0	0	0

Fig. 10. Boundary condition adopted in the 4P bending test.

Table 7
Mechanical properties of the simulated fibula plate with decreasing resisting volume.

Offset [mm]	Volume [%]	Bending Strength [N•m]	Bending Structural Stiffness [N•m^2]
0.000	100.00	2.74	1.30
−0.001	99.91	2.74	1.29
−0.01	99.05	2.69	1.27
−0.1	90.66	2.23	1.02
Minimum acceptable value		**2.3**	**0.17**

Funding

V.V. acknowledges the European Union (NextGeneration EU), for funding PhD Scholarship. M.S. and F.D.F. acknowledge the European Union (NextGeneration EU), for the support through the MUR-PNRR project SAMOTHRACE.

CRediT authorship contribution statement

V. Verro: Writing – original draft, Investigation, Data curation. **F. Di Franco:** Writing – review & editing, Supervision, Methodology, Formal analysis, Data curation. **D. Pupillo:** Investigation, Data curation. **M. Santamaria:** Writing – review & editing, Supervision, Resources, Methodology, Conceptualization.

Declaration of competing interest

The authors declare that they have no known competing financial

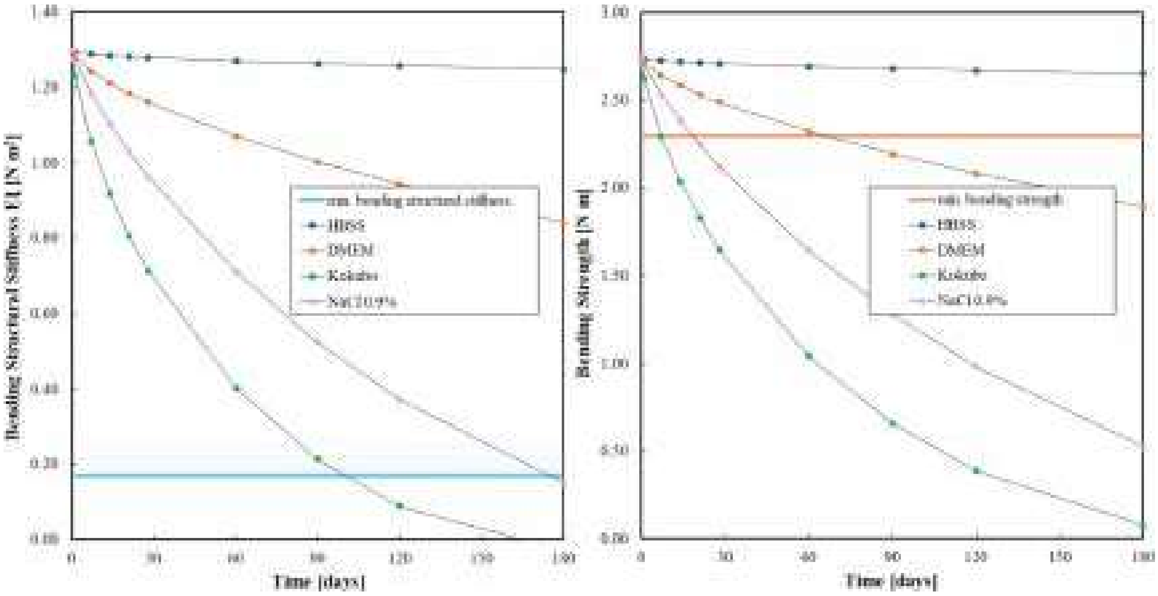

Fig. 11. Estimated mechanical properties of the simulated fibula plate during 180 days immersion in different solutions.

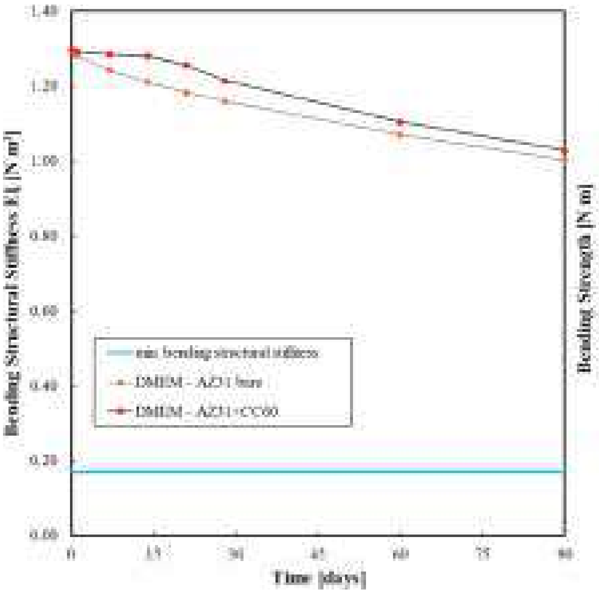

Fig. 12. Estimated mechanical properties of the simulated fibula plate, with and without the stannate based conversion coating, during 90 days immersion in DMEM.

interests or personal relationships that could have appeared to influence the work reported in this paper.

Supplementary materials

Supplementary material associated with this article can be found, in the online version, at doi:10.1016/j.electacta.2025.148093.

Data availability

Data will be made available on request.

References

[1] A. Thakur, A. Kumar, S. Kaya, R. Marzouki, F. Zhang, L. Guo, Recent advancements in surface modification, characterization and functionalization for enhancing the biocompatibility and corrosion resistance of biomedical implants, Coatings 12 (2022), https://doi.org/10.3390/COATINGS12101459.

[2] K.K.A. Mosas, A.R. Chandrasekar, A. Dasan, A. Pakseresht, D. Galusek, Recent advancements in materials and coatings for biomedical implants, Gels. 8 (2022), https://doi.org/10.3390/GELS8050323.

[3] G. Uppal, A. Thakur, A. Chauhan, S. Bala, Magnesium based implants for functional bone tissue regeneration – a review, J. Magnes. Alloys 10 (2022) 356–386, https://doi.org/10.1016/J.JMA.2021.08.017.

[4] M. Sarraf, E. Rezvani Ghomi, S. Alipour, S. Ramakrishna, N. Liana Sukiman, A state-of-the-art review of the fabrication and characteristics of titanium and its alloys for biomedical applications, Biodes. Manuf. 5 (2022) 371–395, https://doi.org/10.1007/S42242-021-00170-3.

[5] R. Davis, A. Singh, M.J. Jackson, R.T. Coelho, D. Prakash, C.P. Charalambous, W. Ahmed, L.R.R. da Silva, A.A. Lawrence, A comprehensive review on metallic implant biomaterials and their subtractive manufacturing, Int. J. Adv. Manuf. Technol. 120 (2022) 1473–1530, https://doi.org/10.1007/S00170-022-08770-8.

[6] A. Bandyopadhyay, I. Mitra, S.B. Goodman, M. Kumar, S. Bose, Improving biocompatibility for next generation of metallic implants, Prog. Mater. Sci. 133 (2023), https://doi.org/10.1016/J.PMATSCI.2022.101053.

[7] S. Hagelstein, S. Zankovic, A. Kovacs, R. Barkhoff, M. Seidenstuecker, Mechanical analysis and corrosion analysis of zinc alloys for bioabsorbable implants for osteosynthesis, Mater. (Basel) 15 (2022) 421, https://doi.org/10.3390/MA15020421, 2022, Vol. 15, Page 421.

[8] E.J. Sim, K. Sakthiabirami, T.G. Jung, S.K. Jo, S.J. Lee, P. Xu, H.K. Sung, E.H. Lee, K.C. Yoon, K.S. Kang, Y.H. Jeong, D.B. Thordarson, C.S. Lee, S.M. Kim, C. Kang, J. H. Song, W.H. Park, Bioabsorbable PLA/PHA composite pins for orthopedic applications: in vitro and in vivo study, J. Ind. Eng. Chem. 146 (2025) 861–870, https://doi.org/10.1016/J.JIEC.2025.03.023.

[9] K. V, N. Kumar B, S. Kumar S, V. M, Magnesium role in additive manufacturing of biomedical implants – challenges and opportunities, Addit. Manuf. 55 (2022), https://doi.org/10.1016/J.ADDMA.2022.102802.

[10] B. Blackman, S. Okunbor, A.M. Sowa, J.M. McDonnell, T.D. Ross, B. Rigney, S. Darwish, J.S. Butler, Bioabsorbable implants are a viable alternative to traditional metallic implants in orthopaedic surgery: a systematic review and meta-analysis, J. Orthop. 65 (2025) 257–269, https://doi.org/10.1016/J.JOR.2025.06.005.

[11] M. Tao, Y. Cui, S. Sun, Y. Zhang, J. Ge, W. Yin, P. Li, Y. Wang, Versatile application of magnesium-related bone implants in the treatment of bone defects, Mater. Today Bio. 31 (2025), https://doi.org/10.1016/J.MTBIO.2025.101635.

[12] V.K. Mahto, A.K. Singh, A. Malik, Surface modification techniques of magnesium-based alloys for implant applications, J. Coat. Technol. Res. 20 (2023) 433–455, https://doi.org/10.1007/S11998-022-00716-9.

[13] J. Liu, F. Shi, S. Ma, J. Sun, S. Liu, W. Ye, Magnesium alloy with superhydrophilic magnesium/gallium-layered double hydroxides coating with antibacterial property as implant material, J. Nanoparticle Res. 27 (2025), https://doi.org/10.1007/S11051-024-06210-0.

[14] M. Nasr Azadani, A. Zahedi, O.K. Bowoto, B.I. Oladapo, A review of current challenges and prospects of magnesium and its alloy for bone implant applications, Prog. Biomater. 11 (2022), https://doi.org/10.1007/S40204-022-00182-X.

[15] H. Delavar, A.J. Mostahsan, H. Ibrahim, Corrosion and corrosion-fatigue behavior of magnesium metal matrix composites for bio-implant applications: a review, J. Magnes. Alloys 11 (2023) 1125–1161, https://doi.org/10.1016/J.JMA.2023.04.010.

[16] T. Wu, K. Zhang, Corrosion and protection of magnesium alloys: recent advances and future perspectives, Coatings 13 (2023) 1533, https://doi.org/10.3390/COATINGS13091533, 2023, Vol. 13, Page 1533.

[17] S. Agarwal, J. Curtin, B. Duffy, S. Jaiswal, Biodegradable magnesium alloys for orthopaedic applications: a review on corrosion, biocompatibility and surface modifications, Mater. Sci. Eng.: C 68 (2016) 948–963, https://doi.org/10.1016/J.MSEC.2016.06.020.

[18] A. Joshi, N. Haththotuwa, J.S. Richard, R. Laven, G.J. Dias, M.P. Staiger, In vitro calibration and in vivo validation of phenomenological corrosion models for resorbable magnesium-based orthopaedic implants, Acta Biomater. 180 (2024) 171–182, https://doi.org/10.1016/J.ACTBIO.2024.03.024.

[19] Y. An, H. Zhang, S. Zhang, Y. Zhang, L. Zheng, X. Chen, W. Tong, J. Xu, L. Qin, Degradation products of magnesium implant synergistically enhance bone regeneration: unraveling the roles of hydrogen gas and alkaline environment, Bioact. Mater. 46 (2025) 331–346, https://doi.org/10.1016/J.BIOACTMAT.2024.12.020.

[20] K.X. Kuah, S. Wijesinghe, D.J. Blackwood, Toward understanding in vivo corrosion: influence of interfacial hydrogen gas build-up on degradation of magnesium alloy implants, J. Biomed. Mater. Res. A 111 (2023) 60–70, https://doi.org/10.1002/JBM.A.37446.

[21] H. Kumar, A.K. Singh, T. Jagadeesha, H.K. Pant, · A. K. Singh, · T. Jagadeesha, A.K. Singh, Biodegradation behavior of magnesium-based biomaterials using surface modification techniques for orthopedic implants: a review, (2025) 53–73. https://doi.org/10.1007/978-3-031-87677-6_6.

[22] J. Xie, T. Zhang, J. Jiang, W. Xue, W. Wang, J. Ni, X. Zhang, X. Liu, Advances in magnesium-based implants for biomedical applications: a comprehensive review and future perspectives, J. Magnes. Alloys (2025), https://doi.org/10.1016/J.JMA.2025.05.009.

[23] A.S. Gnedenkov, S.L. Sinebryukhov, D.V. Mashtalyar, S.V. Gnedenkov, Features of the magnesium alloys corrosion in the chloride-containing media. Solid state phenomena, Trans Tech Publications Ltd, 2014, pp. 143–148, https://doi.org/10.4028/www.scientific.net/SSP.213.143.

[24] M. Kaseem, Y.G. Ko, Morphological modification and corrosion response of MgO and Mg3(PO4)2 composite formed on magnesium alloy, Compos. B Eng. 176 (2019), https://doi.org/10.1016/j.compositesb.2019.107225.

[25] D. Kurchavov, M. Haddad, V. Lair, P. Volovitch, Mg-alloys in water – hydrophilic ionic liquid mixtures: is there a negative difference effect? Corros. Sci. 200 (2022) 110178 https://doi.org/10.1016/J.CORSCI.2022.110178.

[26] A. Nazarov, T. Yurasova, A. Marshakov, Hydrogen absorption and self-corrosion of Mg anode: influence of aqueous electrolyte species, Corros. Mater. Degrad. 5 (2024) 350–369, https://doi.org/10.3390/CMD5030015, 2024, Vol. 5, Pages 350-369.

[27] A.Z. Benbouzid, M.P. Gomes, I. Costa, O. Gharbi, N. Pébère, J.L. Rossi, M.T.T. Tran, B. Tribollet, M. Turmine, V. Vivier, A new look on the corrosion mechanism of magnesium: an EIS investigation at different pH, Corros. Sci. 205 (2022) 110463, https://doi.org/10.1016/J.CORSCI.2022.110463.

[28] L.J. Liu, M. Schlesinger, Corrosion of magnesium and its alloys, Corros. Sci. 51 (2009) 1733–1737, https://doi.org/10.1016/J.CORSCI.2009.04.025.

[29] Z. Shi, M. Liu, A. Atrens, Measurement of the corrosion rate of magnesium alloys using Tafel extrapolation, Corros. Sci. 52 (2010) 579–588, https://doi.org/10.1016/J.CORSCI.2009.10.016.

[30] M. Curioni, L. Salamone, F. Scenini, M. Santamaria, M. Di Natale, A mathematical description accounting for the superfluous hydrogen evolution and the inductive behaviour observed during electrochemical measurements on magnesium, Electrochim. Acta 274 (2018) 343–352, https://doi.org/10.1016/J.ELECTACTA.2018.04.116.

[31] H. Dong, F. Lin, A.R. Boccaccini, S. Virtanen, Corrosion behavior of biodegradable metals in two different simulated physiological solutions: comparison of Mg, Zn and Fe, Corros. Sci. 182 (2021), https://doi.org/10.1016/J.CORSCI.2021.109278.

[32] D. Pupillo, F. Di Franco, L. Iannucci, S. Grassini, S. Virtanen, M. Santamaria, Following Zn corrosion during long term immersion test in physiological solutions to establish the potential of zinc as biodegradable prosthetic material, Electrochim. Acta 531 (2025), https://doi.org/10.1016/J.ELECTACTA.2025.146411.

[33] Practice for Preparing, Cleaning, and evaluating corrosion test specimens, (2017). https://doi.org/10.1520/G0001-03R17E01.

[34] Specification and test method for metallic bone plates, (2024). https://doi.org/10.1520/F0382-24.

[35] Fibula, Multifragmentary fracture: lateral bridging plate, (n.d.). https://surgeryreference.aofoundation.org/orthopedic-trauma/adult-trauma/malleoli/basic-technique/fibula-multifragmentary-fracture-lateral-bridging-plate (accessed July 14, 2025).

[36] AAP Implantate AG | Distal Tibia/Fibula plates 3.5, (n.d.). https://www.aap.de/products/loqteq/ankle-joint/distal-tibia-fibula-plates (accessed July 14, 2025).

[37] LCP™ distal fibula plate system (2.7/3.5 mm) | products | DePuy synthes, (n.d.). https://www.jnjmedtech.com/en-EMEA/product/lcp-distal-fibula-plate-system-2735-mm (accessed July 14, 2025).

[38] M. Liu, Q. Zhang, X. Tang, C. Liu, D. Mei, L. Wang, S. Zhu, M.L. Zheludkevich, S. Lamaka, S. Guan, Effect of medium renewal mode on the degradation behavior of Mg alloys for biomedical applications during the long-term in vitro test, Corros. Sci. 229 (2024), https://doi.org/10.1016/j.corsci.2024.111851.

[39] C. Wang, X. Liu, D. Mei, M. Deng, Y. Zheng, M.L. Zheludkevich, S.V. Lamaka, Local pH and oxygen concentration at the interface of Zn alloys in Tris-HCl or HEPES buffered Hanks' balanced salt solution, Corros. Sci. 197 (2022), https://doi.org/10.1016/j.corsci.2021.110061.

[40] A. Zaffora, F. Di Franco, D. Virtù, F. Carfì Pavia, G. Ghersi, S. Virtanen, M. Santamaria, Tuning of the Mg alloy AZ31 anodizing process for biodegradable implants, ACS. Appl. Mater. Interfaces. 13 (2021) 12866–12876, https://doi.org/10.1021/ACSAMI.0C22933/ASSET/IMAGES/MEDIUM/AM0C22933_M005.GIF.

[41] C.X. Qian, L.Z. Sun, X.N. Yu, Chemosynthesis of nano-magnesium phosphates and its characterization, Dig. J. Nanomater. Biostruct. 11 (2016) 1099–1103. - References - Scientific Research Publishing, (n.d.), https://www.scirp.org/reference/referencespapers?referenceid=3325676. accessed July 26, 2025.

[42] R.J. Sanghavi, S.C. Upadhyay, A. Kumar, Management of solid waste marble powder: improving quality of sodium chloride obtained from sulphate-rich lake/subsoil brines with simultaneous recovery of high-purity gypsum and magnesium carbonate hydrate, Environ. Sci. Pollut. Res. 29 (2022) 40068–40078, https://doi.org/10.1007/S11356-022-18932-6/TABLES/18.

[43] M.E. Orazem, B. Tribollet, Electrochemical impedance spectroscopy, Wiley, 2008, https://doi.org/10.1002/9780470381588.

[44] S. Zhang, Q. Li, B. Chen, X. Yang, Preparation and corrosion resistance studies of nanometric sol-gel-based CeO2 film with a chromium-free pretreatment on AZ91D magnesium alloy, Electrochim. Acta 55 (2010) 870–877, https://doi.org/10.1016/j.electacta.2009.07.053.

[45] A.S. Gnedenkov, Y.I. Kononenko, S.L. Sinebryukhov, V.S. Filonina, I.E. Vyaliy, A. D. Nomerovskii, A.Y. Ustinov, S.V. Gnedenkov, The effect of smart PEO-coatings impregnated with corrosion inhibitors on the protective properties of AlMg3 aluminum alloy, Mater. (Basel) 16 (2023), https://doi.org/10.3390/ma16062215.

[46] A. Cusanno, A. Rizzuti, A. De Bonis, D. Pupillo, M. Curcio, D. Sorgente, M. Santamaria, P. Mastrorilli, G. Palumbo, Pulsed laser deposition and phosphate chemical conversion coatings for tailoring the corrosion behavior of AZ31 resorbable implants manufactured via superplastic forming, Metall. Mater. Trans. B: Process Metall. Mater. Process. Sci. (2025), https://doi.org/10.1007/s11663-025-03849-5.

[47] Orthopedic fracture fixation plates - performance criteria for safety and performance based pathway | FDA. https://www.fda.gov/regulatory-information/search-fda-guidance-documents/orthopedic-fracture-fixation-plates-performance-criteria-safety-and-performance-based-pathway, 2022 accessed July 14, 2025.

[48] V. Verro, F. Di Franco, F. Carfì Pavia, F. La Monica, M. Santamaria, Chemical and electrochemical surface treatments to grow magnesium hydroxystannate/manganese stearate coating for tuning biodegradation rate of AZ31 for bioresorbable implants, Electrochim. Acta 525 (2025), https://doi.org/10.1016/j.electacta.2025.146159.